1   **High-resolution cryo-EM structure of photosystem II: Effects of electron beam**

2   **damage**

3   Koji Kato[1,4], Naoyuki Miyazaki[2,4], Tasuku Hamaguchi[3,4], Yoshiki Nakajima[1], Fusamichi

4   Akita[1,*], Koji Yonekura[3,*] and Jian-Ren Shen[1,*]

5

6   [1] *Research Institute for Interdisciplinary Science and Graduate School of Natural*

7   *Science and Technology, Okayama University, 3-1-1 Tsushima Naka, Okayama*

8   *700-8530, Japan*

9   [2] *Life Science Center for Survival Dynamics, Tsukuba Advanced Research Alliance*

10   *(TARA), University of Tsukuba, Ibaraki 305-8577, Japan*

11   [3] *Biostructural Mechanism Laboratory, RIKEN Spring-8 Center, 1-1-1 Kouto, Sayo-cho,*

12   *Sayo-gun, Hyogo 679-5148, Japan*

13

14   [4] These authors contributed equally to this work.

15

16   *Corresponding Authors:

17   Fusamichi Akita, E-mail: fusamichi_a@okayama-u.ac.jp

18   Koji Yonekura, E-mail: yone@spring8.or.jp

19   Jian-Ren Shen, E-mail: shen@cc.okayama-u.ac.jp

20

21

22

23

24   **Abstract**

25   Photosystem II (PSII) plays a key role in water-splitting and oxygen evolution. X-ray

26   crystallography has revealed its atomic structure and some intermediate structures.

27   However, these structures are in the crystalline state, and its final state structure has not

28   been solved because of the low efficiencies of the S-state transitions in the crystals. Here

29   we analyzed the structure of PSII in solution at 1.95 Å resolution by single-particle

30   cryo-electron microscopy (cryo-EM). The structure obtained is similar to the crystal

31   structure, but a PsbY subunit was visible in the cryo-EM structure, indicating that it

32   represents its physiological state more closely. Electron beam damage was observed at a

33   high-dose in the regions that were easily affected by redox states, which was reduced by

34   reducing the electron dose. This study will serve as a good indicator for determining

35   damage-free cryo-EM structures of not only PSII but also all biological samples,

36   especially redox-active metalloproteins.

37

38

Introduction

39

40   PSII is a multi-subunit pigment-protein complex embedded in the thylakoid

41   membranes of higher plants, green algae and cyanobacteria, and is the only molecular

42   machine capable of oxidizing water by use of visible light in the nature. Water molecules

43   are split into electrons, hydrogen atoms and oxygen molecules at the catalytic center of

44   PSII, namely, the oxygen-evolving complex (OEC), through four electron and/or proton

45   removing steps as described in the Si-state cycle (with i = 0–4, where i indicates the

46   number of oxidative equivalents accumulated)[1].

47   In order to elucidate the mechanism of the water-splitting reaction, the structure of

48   PSII has been studied extensively by X-ray diffraction (XRD) with synchrotron radiation

49   (SR)[2-6]. The SR structure of PSII at an atomic resolution revealed that OEC is a Mn_4CaO_5

50   cluster organized into a distorted-chair form, in which the cuboidal part is composed of

51   Mn_3CaO_4 and the outer manganese is attached to the cuboid via two μ-oxo-bridges[6].

52   However, based on the extended X-ray absorption fluorescence spectra (EXAFS)

53   analysis, the dose used for collecting the SR structure at 1.9 Å resolution may cause 25%

54   of the Mn ions in OEC to be reduced to 2^+ ions, causing some elongations in the Mn-Mn

55   distances in the structure[7]. This issue is overcome by the use of X-ray free electron lasers

56   (XFEL), which provide X-ray pulses with ultra-short durations that enable collection of

57   the diffraction data before onset of the radiation damage (diffraction before destruction)[8].

58   Using XFELs, radiation damage free structure of PSII was solved at a high resolution by

59   an approach called fixed-target serial rotational crystallography, which uses multiple

60   large PSII crystals by a shot-and-move/rotation method[9,10]. The result showed a

3

61   shortening of 0.1-0.2 Å in some of the Mn-Mn distances, indicating that the structure

62   represents a damage free one[10]. By a combination of serial femtosecond X-ray

63   crystallography (SFX) with XFELs and small crystals, structures of S-state intermediates

64   up to S_3-state were analyzed by pump-probe experiments where snapshot diffraction

65   images were collected from flash-illuminated PSII crystals[11-14]. These results

66   demonstrated the appearance of a new oxygen atom O6 (Ox) close to O5 between Mn1

67   and Mn4 upon two flashes, suggesting insertion of a water molecule in the $S_2 \rightarrow S_3$

68   transition for O=O bond formation. However, all these studies were conducted with PSII

69   crystals, and the efficiencies of the S-state transitions in the microcrystals were reported

70   to be slightly lower compared with those in solution using light-induced Fourier

71   transform infrared difference spectroscopy[15]. Moreover, it is unknown if the structure of

72   PSII in the crystalline state is the same as those in the solution.

73   Cryo-electron microscopy (cryo-EM) can solve the structures of proteins in solution

74   without crystallization, which may represent the physiological states of proteins more

75   closely. It can also analyze the dynamic changes of proteins in solutions in the time range

76   of ms, provided that cooling of the samples is rapid enough. In recent years, the technique

77   of cryo-EM has been developed rapidly, and the resolutions of structures that can be

78   solved by cryo-EM are increased dramatically[16-18]. However, there is also the issue of

79   damage caused by the electron beam during cryo-EM data collection, even though the

80   cryo-EM is usually conducted at a low temperature. Radiation damage has been

81   extensively studied with X-rays, and it has been shown that the damage mainly manifests

82   as breakage of disulfide bonds, decarboxylation of acidic amino and photoreduction of

4

83   metal centers[7,19-21]. The damage caused by electron beams have also been shown in

84   cryo-EM analysis[17]. In order to obtain a high resolution, however, cryo-EM studies are

85   usually conducted at a high-dose of electron beams without paying much attention to the

86   electron beam damage. In this paper, we analyzed the structure of PSII in ice by cryo-EM

87   at a resolution of 1.95 Å, and investigated the electron beam damage to PSII, especially

88   its OEC, upon dose accumulation. We show that the structure of PSII analyzed by cro-EM

89   may represent the physiological state more closely, as it retains the PsbY subunit.

90   However, it suffers from a severe electron beam damage at a high-dose, and this damage

91   was reduced at a much decreased dose without a significant loss of resolution. These

92   results are not only important for the analysis of the PSII structure in solution, but also

93   provide important implications for all cryo-EM studies that use considerably high-doses

94   for imaging.

95

96   **Result**

97   **High resolution single particle analysis of the PSII**

98   To obtain the high resolution structure of PSII, three data sets of single-particle

99   images of the PSII dimer from *T. vulcanus* were collected using Thermo Fisher Scientific

100   Titan Krios and JEOL CRYO ARM 300 at different conditions as summarized in Table 1.

101   Because the sample for the 75 x k magnification using Titan contained 5% glycerol in the

102   buffer, the sample was diluted ten times with the buffer without glycerol. The other

103   samples did not contain the glycerol and were concentrated by PEG 1450 precipitation in

104   the final step. Image processing yielded final resolutions of 2.22 Å for the data set

5

105   collected at 75 x k magnification using Titan Krios (Titan-75k), 2.20 Å for the data set

106   collected at 96 x k magnification using Titan Krios (Titan-96k), and 1.95 Å for the data

107   set collected at 60 x k magnification using CRYO ARM 300 (ARM-60k) (Table 1, Table

108   2 and Supplementary Fig. 1-4). These results indicate that the quality of the cryo-EM

109   density maps achieved were at the level comparable to those obtained with SR and XFEL

110   previously[6,10]. The resolutions of the Titan-75k and Titan-96k data were almost the same,

111   in spite of the different magnifications and buffers used. The resolution of the ARM-60k

112   data was significantly better than that of the Titan-96k data, despite that the same buffer

113   condition was used for the two data sets. The resolution achieved by cryo-EM depends on

114   a number of factors, including sample quality, the type and preparations of cryo-grids

115   used, the thickness of ice in the samples, microscope alignment and imaging conditions,

116   etc. However, the major one could be the electron beam source. The CRYO ARM 300

117   microscope has a cold field emission gun (CFEG) that produces an electron beam with a

118   high temporal-coherence and superior high-resolution signals[22] over that from the

119   Schottky emission gun equipped in the Krios microscope.

120   In Fig. 1, the squared inverse resolution of reconstructions achieved from random

121   subsets of particles is plotted against the subset size on a logarithmic scale. This is known

122   as Rosenthal-Henderson plot[23]. These plots indicated that the resolution is proportional to

123   the log of particle size. The B-factors estimated from these plots are 60.8 for the

124   Titan-75k data set, 74.9 for the Titan-96k data set and 43.3 $Å^2$ for the ARM-60k data set.

125   The ARM-60k data set again shows the lowest value, in agreement with its highest

126   resolution.

127

128   **Overall structure of PSII**

129   The overall atomic model of PSII was built based on the highest 1.95-Å resolution

130   density map reconstructed from the ARM-60k data set. At this resolution, the features of

131   cofactors and water molecules can be easily identified in the map (Fig. 2). The overall

132   architecture of the PSII dimer from *T. vulcanus* is very similar to that of SR (PDB:

133   3WU2)[6] and XFEL structures (PDB: 4UB6 and 4UB8)[10], except for PsbY. The density of

134   PsbY is present in one of the two monomers in the native (PDB: 4UB6)[10] and the

135   Sr^{2+}-substituted PSII dimer structures (PDB: 4IL6)[24] but absent in the SR structure (PDB:

136   3WU2)[6]. However, this density was seen in both sides of the PSII dimer in the cryo-EM

137   structure, although the density is somewhat poorer compared with that of the other

138   assigned subunits (Fig. 2a, f). This suggests that the cryo-EM structure more closely

139   represents the native state of PSII.

140   The root mean square deviation (RMSD) is 0.40 Å for 5227 C_α atoms between the

141   structures of cryo-EM and SR, and 0.46 Å for 5267 C_α atoms between the structures of

142   cryo-EM and XFEL. Because the RMSD was 0.32 Å for 5241 C_α atoms between the SR

143   and XFEL structures of PSII dimers, the cryo-EM structure is almost identical to the SR

144   and XFEL structures at the backbone level. In the cryo-EM density map, we assigned

145   2432 water molecules at a contour level of 5 σ, which are slightly less than the number of

146   waters assigned in the SR and XFEL structures[6,10]. The atomic displacement parameter

147   (ADP) of the cryo-EM structure refined with Refmac5 in reciprocal space correlated well

148   with that of the SR structure (Supplementary Fig. 5), although it may be somewhat

149   overestimated in the cryo-EM structure. Since the cryo-EM map was subjected to

150   B-factor sharpening with Postprocessing, it is not suitable to compare ADP values

151   directly between cryo-EM and X-ray structures. Nevertheless, the relative ADP of the

152   atoms in the molecule appears to reflect the characteristics of the map. The average ADP

153   for the OEC atoms (13.8 $Å^2$) were found to be lower than that observed in the overall

154   protein atoms of the cryo-EM structure (20.6 $Å^2$), suggesting that the structure of OEC

155   was determined more reliably than that of the overall structure. This may be due to the

156   presence of metal ions in the Mn_4CaO_5 cluster, which gives rise to higher cryo-EM

157   density than that of lighter protein atoms.

158

159   **Electron beam damage to the PSII structure**

160   Several regions of PSII were found to have different structures between cryo-EM

161   and XFEL, which are considered to arise from electron beam induced damage. In the

162   PsbO subunit, a disulfide bond between Cys19 and Csy41 was observed in the XFEL

163   structure[10], but it was completely cleaved in the cryo-EM structure (Fig. 3a). In the C

164   terminus of D1 subunit, a part of Ala344, the C-terminal residue that coordinated to the

165   Mn_4CaO_5 cluster, flipped out from the OEC and adopted an alternative conformation in

166   the cryo-EM structure (Fig. 3b). These are the typical sign of damage caused by the

167   electron beam irradiation during the acquirement of cryo-EM images.

168   In the OEC, the positions of heavy metals were confirmed clearly and were assigned

169   based on their highest peaks in the cryo-EM map achieved at the high-dose (Fig. 4a). In

170   addition, five oxo-oxygen atoms and four water molecules ligated to the OEC were

8

171   assigned in the difference map, which were obtained by subtracting the metal densities in

172   a diameter of 1.5 Å of that metal from the whole cryo-EM map. The overall architecture

173   of the OEC in the cryo-EM structure is very similar to that of the SR and XFEL structures,

174   however, distinct differences were observed in Mn–Mn and Mn–O distances (Table 3).

175   The Mn–Mn distances calculated from the initially assigned positions based on the

176   cryo-EM density were 2.8 Å for Mn1–Mn2, 3.5 Å for Mn1–Mn3, 5.0 Å for Mn1–Mn4,

177   3.1 Å for Mn2–Mn3, 5.4 Å for Mn2–Mn4, and 2.7 Å for Mn3–Mn4 (Table 3). Except the

178   Mn1-Mn4 and Mn3-Mn4 distances, all of the Mn-Mn distances are 0.1-0.2 Å and 0.1–0.4

179   Å longer than those of the SR and XFEL structures, respectively[6,10]. Most of the Mn-O

180   distances in the cryo-EM structure were also 0.1-0.5 Å and 0.1–0.7 Å longer than those in

181   the SR and XFEL structures, respectively (Table 3)[6,10]. These differences may be caused

182   by two factors. One is the electron beam damage, and the other one is the experimental

183   errors in determining the positions of the individual atoms based on the cryo-EM map

184   only. Especially, the position of oxygen atoms may not be determined precisely because

185   the map of the oxygen atoms cannot be separated from the map of metal atoms. Thus, the

186   OEC structure was refined with the restraints for bond distances (Mn–O and Ca–O) that

187   were taken from the initial positions. The Mn–Mn distances refined with restraints were

188   2.8 Å for Mn1–Mn2, 3.4 Å for Mn1–Mn3, 5.0 Å for Mn1–Mn4, 3.1 Å for Mn2–Mn3, 5.6

189   Å for Mn2–Mn4, and 3.0 Å for Mn3–Mn4 (Fig. 4b and Table 3). Except the Mn1-Mn4

190   distance, all of the Mn-Mn distances are still 0.1-0.2 Å and 0.1–0.4 Å longer than those of

191   the SR and XFEL structures, respectively[6,10]. Most of the Mn-O distances in the cryo-EM

192   structure refined with the restraints were also 0.1–0.4 Å longer than those in the SR and

9

193   XFEL structures (Table 3). In addition, the occupancy of the OEC atoms refined with

194   Refmac5 were found to be lower than 1.0 (0.87). These results indicate that the OEC is

195   reduced by electron dose exposed, leading to the elongation of the Mn-Mn and Mn-O

196   distances and some disorder or displacement of the metal centers during the cryo-EM

197   data acquisition. This reduced occupancy is in agreement with the previous theoretical

198   calculation of the cryo-EM structure of higher plant PSII-LHCII supercomplex[25], which

199   may be the reason why a part of Ala344 flipped out and does not ligate to the OEC. The

200   reduction of metal ions with electron doses was already observed in electron

201   crystallography previously[26].

202   Further structural changes in the redox-active sites, including reaction center

203   chlorophylls, electron transfer chain, proton channels and water channels, were not found

204   except the water molecule near D2-Tyr160 (Y_D) (Supplementary Fig. 6c). This water

205   molecule was disordered at two positions with one being able to hydrogen bond to Y_D and

206   the other one being able to hydrogen bond to D2-Arg180 in the SR structure and XFEL

207   structures[6,10]. In the cryo-EM structure, this water molecule was ordered and connected to

208   D2-Arg180. This may reflect the electron beam induced damage, which causes reduction

209   of Y_D and broken the hydrogen-bond to Y_D^+.

210

211   **Reducing electron beam dosage in determining the PSII structure**

212   In order to reduce the electron beam damage, the final cryo-EM maps were

213   calculated from only initial several frames of each movie stack. In Supplementary Fig. 7,

214   the inverse resolutions of reconstructions achieved from decreased electron doses for the

215   ARM-60k data set, associated with the frame numbers, are plotted against the dose values

216   on a logarithmic scale. Surprisingly, the electron doses from 83 e$^-$ Å^{-2} down to 10 e$^-$ Å^{-2}

217   gave rise to almost the same resolution, indicating that increase in the electron beam

218   dosage during this range does not contribute to increase in the resolution significantly.

219   Near atomic resolution is retained at the total dose of 3.3 e$^-$ Å^{-2} for the ARM-60k data set

220   (2.08 Å), which was achieved by using the initial 2 frames of each micrograph.

221   An overall atomic model of the low-dose PSII was built based on the highest 2.08 Å

222   resolution density reconstructed from the ARM-60k data set at the dose of 3.3 e$^-$ Å^{-2}

223   (Table 2). The overall architecture of the low-dose PSII is very similar to that of the

224   high-dose PSII, with a RMSD of 0.21 Å for 5310 C_α atoms between the structures of

225   high-dose and low-dose. However, in the regions where structural changes were observed

226   due to electron beam damage, the disulfide bond between Cys19 and Csy41 of the PsbO

227   was restored at a dose of 5 e$^-$ Å^{-2}, and Ala344 of the D1 subunit was returned to the single

228   conformation to ligate to the OEC similar to those seen in the crystal structures (Fig. 3, 4

229   and 5, Supplementary Fig. 6 and 8). The ADP for the OEC atoms (12.8 Å^2) were lower

230   than that observed in the overall protein atoms of the cryo-EM structure (22.4 Å^2), and the

231   occupancy value of the OEC atoms refined with Refmac5 was returned to 1.0. These

232   results indicate the reduction of the electron beam damage in the structure. However,

233   similar to the high-dose structure, the water molecule near Y_D are connected to

234   D2-Arg180 in an ordered manner and not hydrogen-bonded to Y_D (Supplementary Fig. 6),

235   indicating that some electron beam damage remained.

236   The Mn–Mn distances calculated from the initially assigned positions based on the

11

237   cryo-EM density were 3.0 Å for Mn1–Mn2, 3.4 Å for Mn1–Mn3, 5.3 Å for Mn1–Mn4,

238   2.8 Å for Mn2–Mn3, 5.4 Å for Mn2–Mn4, and 3.1 Å for Mn3–Mn4 (Table 3). All of these

239   Mn-Mn distances are 0.1–0.3 Å longer than those of the SR and XFEL structures[6,10].

240   Most of the Mn-O distances in the cryo-EM structure were also 0.1–0.6 Å and 0.1–0.8 Å

241   longer than those in the SR and XFEL structures, respectively (Table 3). As is done with

242   the high-dose structure, we refined the OEC structure with the restraints for bond

243   distances of Mn–O and Ca–O that were taken from the initial positions. The Mn–Mn

244   distances in the OEC refined with the restraints were 2.9 Å for Mn1–Mn2, 3.2 Å for

245   Mn1–Mn3, 5.1 Å for Mn1–Mn4, 2.9 Å for Mn2–Mn3, 5.4 Å for Mn2–Mn4, and 3.0 Å for

246   Mn3–Mn4 (Fig. 4f, Table 3). Most of these distances are shorter than those of the

247   high-dose structure and close to those of the XFEL structure, although most of them are

248   still longer than the SR and XFEL structures by 0.1 Å and 0.1-0.2 Å, respectively (Table

249   3). The Mn-O distances after refinement with the restraints also became close to the

250   XFEL structure, indicating the necessity of refinement with restraints. However, some of

251   the Mn-O distances were still longer or deviated from those found in the XFEL structure,

252   which may be caused by the electron beam damage remained and/or coordinate errors in

253   the cryo-EM analysis at the current resolution.

254

255   **Discussion**

256   In recent years, the resolution of single-particle cryo-EM has improved to atomic

257   resolutions without crystallization, and it has been reported that biological samples are

258   damaged by electron beams. In this study we elucidated the structure of the PSII at 1.95 Å

259   resolution in solution by cryo-EM, which is similar to the SR or XFEL structure in the

260   crystalline state except the PsbY subunit, which was visible in the cryo-EM structure but

261   absent or partially visible in the SR and XFEL structures[6,10]. This indicates that the

262   structure solved by cryo-EM more closely represents the physiological state.

263   Despite the total electron dose of 83 e$^-$ Å^{-2} which is commonly used in the acquisition

264   of cryo-EM images, radiation damages are found in regions susceptible to redox changes,

265   i.e. the disulfide bond and the redox-active metals, whereas the overall structure is very

266   similar to those of the SR and XFEL structures[6,10]. The exposure of the sample to a flux of

267   electrons is conveniently expressed in terms of electrons per Å^2 of specimen surface area

268   (e$^-$ Å^{-2}), which is converted to the SI unit for the absorbed ionizing radiation, the Gray (Gy,

269   with 1 Gy = 1J kg^{-1}), by a factor of □3.7[27]. Thus, the total electron dose of 83 e$^-$ Å^{-2} is

270   equal to the absorption of 307 MGy, which greatly exceeds the Henderson limit (20

271   MGy) that is the X-ray dose that a cryo-cooled crystal can absorb before the diffraction

272   pattern decays to half of its original intensity[28]. Nevertheless, our cryo-EM structure is

273   almost the same to the SR and XFEL structures in the redox-active sites, including

274   reaction center chlorophylls, electron transfer chain, proton channels and water channels,

275   indicating that the radiation damage does not affect the structure significantly. This is

276   considered to be the result of successful dose-weighted correction in the Bayesian

277   polishing step. However, in the PsbO subunit, disulfide bond between Cys19 and Csy41

278   were completely breaking (Fig. 3) in the cryo-EM structure. In the OEC structure, the

279   Mn-Mn were 0.1–0.4 Å longer than those in the XFEL structure, and most of the Mn-O

280   distances were also significantly longer. In addition, the occupancy of the OEC atoms

281 were lower than 1.0 (0.87), resulting in a multiple conformation of the C-terminal residue

282 of D1, where a part of Ala344 flipped to a direction that does not ligate to the OEC.

283 We examined whether radiation damage could be reduced by reducing the total

284 number of stacked movie frames used in the structural analysis. In the electron doses

285 analyzed, the reconstructed map from summing the initial two frames of each micrograph

286 (3 e$^-$ Å^{-2}, 11.1 MGy) gave rise to almost similar resolutions to that of high-dose data set

287 (83 e$^-$ Å^{-2}, 307 MGy) (Supplementry Fig.7). The reconstructed map from the ARM-60k

288 data set at the dose of 3.3 e$^-$ Å^{-2} (11.1 MGy) gave a resolution of 2.08 Å. This structure

289 was compared with that obtained with the high-dose, and it was found that the disulfide

290 bond in the PsbO was recovered, and Ala344 of the D1 subunit was returned to the single

291 conformation similar to the SR and XFEL structures (Fig. 3 and 5). This indicates a

292 significant reduction of the electron beam damage to the structure. In the structure of

293 OEC, most of the Mn-Mn and Mn-O distances became shorter than those observed in the

294 high-dose structure before refinement. However, some of them are still significantly

295 deviated from those of the XFEL structure (Table 3), which become closer after the

296 refinement with restraints starting from the initial structure. Thus, it is advisable to refine

297 the cryo-EM structure with restraints imposed for compounds such as the Mn_4CaO_5

298 cluster.

299 After refinement, most of the Mn-Mn and Mn-O distances of the low-dose structure

300 are similar to those observed in the XFEL structure. However, some of the distances are

301 still longer than or deviated from those found in the damage free XFEL structure[10]. This

302 may be caused by two reasons; one is some electron beam damage remained, and the

14

303   other one is coordinate errors existed in the cryo-EM structure. It has been reported that

304   about 80% of Mn of OEC in solution is reduced to divalent cations by an X-ray dose of 5

305   MGy[7]. Even though it is estimated that about 90% of Mn of OEC is Mn(II) at an electron

306   beam dose of 11.1 MGy used for the low-dose structure, the structure of the OEC retained

307   an occupancy of 1.0. This may be contributed by the stability of the structure of OEC, as

308   the metal ions of OEC are liganded by seven amino acid residues (D1-D170, D1-E189,

309   D1-H332, D1-E333, D1-D342, D1-A344, and CP43-E354). However, the longer

310   distances observed in some of the metal-oxygen distances of OEC even in the low-dose

311   structure indicated the existence of electron beam damage. Tanaka et al. has reported that,

312   using SR, a dose of 0.1 MGy is necessary to achieve a structure similar to that of the

313   XFEL structure[29]. Thus, in order to achieve a damage free structure, the electron beam

314   dose needs to be further reduced. Fortunately, our data indicated that the resolution

315   depends on the particles used, and by using more images and particles, it will be possible

316   to lower the electron beam dose and achieve the structure at a higher resolution.

317   Coordinate errors in the cryo-EM structure may be caused by the ambiguities in the

318   orientations of particles and their averaging, as well as the subsequent structural analysis

319   procedures. Structural analysis by cryo-EM at a higher resolution should eliminate such

320   errors, and gives rise to a more accurate structure. It is also expected that improvements in

321   the averaging and structural analysis algorithms of the cryo-EM data may improve the

322   accuracy of the structures at the same resolutions.

323   In summary, we show that the electron dose commonly used in cryo-EM is damaging

324   to protein samples. However, the damaged area was limited to redox-sensitive part. Our

15

325   results suggest that it is possible to obtain a structure with less damage and high

326   resolution by reducing the total dose and increasing the number of particles. This study

327   will serve as a good indicator for determining damage-less cryo-EM structures of PSII

328   and all biological samples, especially redox-active metalloproteins.

329

330

331   **Methods**

332   **Growth of cells and purification of PSII.** Cells of *Thermosynechococcus vulcanus* (*T.*

333   *vulcanus*) were grown in four 10 L bottles at 50°C. PSII with a high oxygen evolving

334   activity was purified from *T. vulcanus* as described previously[30-32] and suspended with a

335   buffer containing 20 mM MES-NaOH (pH 6.0), 0.04% β-dodecyl-D-maltopyranoside

336   and 5% glycerol. For the Titan-96k and ARM-60k data collection, glycerol in the buffer

337   was removed by polyethylene glycol (PEG) precipitation and the resultant PSII was

338   re-suspended in a buffer containing 20 mM MES-NaOH (pH 6.0), 20 mM NaCl, 3 mM

339    $CaCl_2$, 0.04% β-dodecyl-D-maltopyranoside.

340

341   **Cryo-EM data collection.** For cryo-EM experiments, 3-μL aliquots of the PSII sample

342   at each condition (shown in Table 1) were applied to Quantifoil R1.2/1.3, Mo 300 mesh

343   or Cu 200 mesh grids. The grids were incubated for 10 s in an FEI Vitrobot Mark IV at

344   4°C and 100% humidity. The grids were immediately plunged into liquid ethane cooled

345   by liquid nitrogen and then transferred into the Titan Krios (Thermo Fischer Scientific)

346   equipped with a field emission gun, a Cs corrector (CEOS GmbH), and a direct electron

347   detection camera (Falcon 3EC, Thermo Fischer Scientific), or CRYO ARM 300 (JEOL)

348   equipped with a cold-field emission gun and a direct electron detection camera (Gatan K2

349   summit, Gatan Inc). These microscopes were operated at 300 kV and a nominal

350   magnification of $\times$ 75,000 (Titan-75k), $\times$ 96,000 (Titan-96k) for Titan Krios and $\times$ 60,000

351   (ARM-60k) for CRYO ARM 300. Images were recorded using the Falcon 3EC in linear

352   mode or Gatan K2 summit in counting mode. Micrographs were recorded with a pixel

353   size of 0.870 Å, 0.678 Å and 0.822 Å at a dose rate of 40 electrons $Å^{-2}$ sec^{-1}, 40 electrons

354     $Å^{-2}$ sec^{-1} and 83 electrons $Å^{-2}$ sec^{-1} for Titan-75k, Titan-96k and ARM-60k, respectively.

355   The nominal defocus range were −1.0 to −2.0 μm, −1.0 to −2.5 μm, and −0.8 to −1.6 μm

356   for Titan-75k, Titan-96k and ARM-60k, respectively. Each exposure was conducted for

357   45.11 s, 26.64 s and 10.00 s, and were dose-fractionated into 78, 39 and 50 movie frames

358   for Titan-75k, Titan-96k and ARM-60k, respectively. We acquired 2,084, 4,237 and

359   2,160 images for the data sets of Titan-75k, Titan-96k and ARM-60k, respectively.

360

361   **Cryo-EM image processing.** Movie frames were aligned and summed using the

362   MotionCor2 software[33] to obtain a final dose weighted image. Estimation of the contrast

363   transfer function (CTF) was performed using the CTFFIND4 program[34]. All of the

364   following processes were performed using RELION3.0[35]. For structural analyses of the

365   Titan-75k data set, 354,233 particles were automatically picked from 2,084 micrographs

366   and then were used for reference-free 2D classification. Then, 309,028 particles were

367   selected from the good 2D classes and subjected to 3D classification with a C2 symmetry.

368   The 1.9 Å PSII structure from *T. vulcanus* (PDB: 3WU2)[6] was employed for the initial

369   model for the first 3D classification with 60-Å low-pass filter. As shown in the

370   Supplementary Fig. 1 and 2, the PSII structure was reconstructed from 90,897 particles at

371   an overall resolution of 2.22 Å. For structural analyses of the Titan-96k data set, 612,287

372   particles were automatically picked from 4,237 micrographs and then used for

373   reference-free 2D classification. Then, 566,145 particles were selected from the good 2D

374   classes and subjected to 3D classification with a C2 symmetry. The 2.22-Å map from

375   Titan-75k data was employed for the initial model for the first 3D classification with a

376   60-Å low-pass filter. As shown in the Supplementary Fig. 1 and 2, the PSII structure was

377   reconstructed from 203,912 particles at an overall resolution of 2.20 Å. For structural

378   analyses of the ARM-60k data set, 481,946 particles were automatically picked from

379   2,160 micrographs and used for reference-free 2D classification. Then, 481,927 particles

380   were selected from the good 2D classes and subjected to 3D classification with a C2

381   symmetry. The 2.22-Å map from Titan-75k data was employed for the initial model for

382   the first 3D classification with a 60-Å low-pass filter. The PSII structure was

383   reconstructed from 174,099 particles at an overall resolution of 1.95 Å (Supplementary

384   Fig. 3 and 4). For the low-dose maps, the summing number of movie frames were

385   decreased in the final step of Bayesian polishing and used for reconstruction without

386   refinement of particle positions and orientations, using RELION[35] with the command line

387   option "relion_reconstruct" and then post-processed in RELION[35]. All of the resolution

388   was estimated by the gold-standard Fourier shell correlation (FSC) curve with a cut-off

389   value of 0.143 (Supplementary Fig. 2 and 4)[36]. The local resolution was estimated using

390   RELION[35].

391

392   **B-factor estimation.** For the B-factor plot, the total set of all particles from the final

393   refinement was randomly resampled into smaller subsets. These subsets were subjected

394   to 3D auto-refinement and the resulting orientations were used to calculate

395   reconstructions for each of the two random halves used in the auto-refinement. The

396   squared values of the resulted, estimated resolutions were then plotted against the natural

397   logarithm of the number of particles in the subset, and B-factors were calculated from the

398   slope of the straight line best fitted with the points in the plot (Fig.1).

399

400   **Model building and refinement.** The 1.95-Å and 2.08-Å cryo-EM maps were used for

401   model building of the high-dose and low-dose PSII structures, respectively. First, the

402   crystal structure of *T. vulcanus* PSII (PDB: 3WU2) was manually fitted into each

403   cryo-EM map using UCSF Chimera[37], and then the structures were inspected and

404   adjusted individually with COOT[38]. The structures of high-dose PSII and low-dose PSII

405   were then refined with phenix.real_space_refine[39] and Refmac5[40] with geometric

406   restraints for the protein–cofactor coordination. The positions of four manganese atoms

407   and one calcium atom were clearly visible in the cryo-EM map (Fig. 2 and 4). The

408   positions of the five oxo-oxygen atoms and four water molecules ligated to the OEC were

409   less clear, and they were identified by the difference map in which, the maps of metal ions

410   with a diameter of 1.5 Å from that metal ion were subtracted from the whole cryo-EM

411   map, after placement of the manganese and calcium atoms (Fig. 2 and 4). The initial

412   positions of metal and oxygen atoms were assigned based on the highest peaks in the

19

413   cryo-EM maps. This was taken as the initial structure. Subsequently, we performed the

414   structural refinement with loose restraints (0.1 σ) for bond distances (Mn–O and Ca–O)

415   that were taken from the initial position. Then the refinement was performed with tighter

416   restraints (0.05 σ) for bond distances successively using the modified 'new' library for the

417   bond distances. This geometry optimization procedure was repeated several times until

418   the bond distances converged. However, the distance of Mn4-O4 in the high-dose

419   structure, and the distances of Mn1-O1 and Mn3-O2 in the low-dose structure, were fixed

420   to 1.8 Å, because these distances were too close and could not be refined. The averages of

421   the distances of Mn–Mn, Mn–Ca, Mn–O and Mn–ligand were calculated from each PSIIs

422   in the final four refinement steps and are listed in Table 3. The final models were further

423   validated with Q-score[41], MolProbity[42] and EMringer[43]. The statistics for all data

424   collection and structure refinement are summarized in Table 1 and 2. All structural

425   figures are made by Pymol[44] or UCSF ChimeraX[45].

426

427   **Difference map analysis between low-dose PSII and high-dose PSII.** A difference

428   map was calculated by subtracting high-dose map from the low-dose map, i.e. (low-dose

429   PSII) minus (high-dose PSII). The rotational and translational matrix was calculated

430   based on the refined atomic coordinates using lsqkab in CCP4[46]. A map of low-dose PSII

431   was superposed with a map of high-dose PSII which were applied by a low-pass filter and

432   adjusted to 2.08 Å resolution, with calculated rotational and translational matrix using

433   maprot in CCP4[47]. The high-dose PSII map and the low-dose PSII map was normalized

434   based on the ratio of the root mean square map density value and then the difference maps

435 were calculated using UCSF Chimera[37] with the command line option "vop subtract"

436 (Supplementary Fig. 8).

437

438 **Data availability.** Atomic coordinates and cyro-EM maps for the reported structure of

439 PSII determined from the high-dose data set of ARM-60K and low-dose data set of

440 ARM-60k were deposited in the Protein Data Bank under an accession codes 7D1T and

441 7D1U, respectively, and in the Electron Microscopy Data Bank under the accession codes

442 EMD-30547, EMD-30548, respectively. The cryo-EM maps of the Titan-75k data set and

443 Titan-96k data set were deposited in the Electron Microscopy Data Bank under the

444 accession codes EMD-30549 and EMD-30550, respectively.

445

446

447 **Acknowledgements**

454

455 **Author Contributions**

456 J.-R.S. and K. Y. conceived the project; Y.N. and F.A. purified the PSII; N.M. and T.H.

457   collected cryo-EM images; N. M., K.K. and T.H. processed the EM data. K.K. built the

458   structure model and refined the final models; K.K. analyzed the structure; and K.K., T.H.,

459   N.M. and J.-R.S. wrote the paper, and all of the authors joined the discussion of the

460   results.

461

462

References

1. Kok, B., Forbush, B., & McGloin, M. Cooperation of charges in photosynthetic oxygen evolution. I. A linear four step mechanism. *Photochem. Photobiol.* **11,** 457-475 (1970).

2. Zouni, A. et al. Crystal structure of photosystem II from *Synechococcus elongatus* 3.8 Å resolution. *Nature* **409**, 739-743 (2001).

3. Kamiya, N. & Shen, J.-R. Crystal structure of oxygen-evolving photosystem II from *Thermosynechococcus vulcanus* at 3.7-Å resolution. *Proc. Natl Acad. Sci. USA* **100**, 98–103 (2003).

4. Ferreira, K. N.et al. Architecture of the photosynthetic oxygen-evolving center. *Science* **303**, 1831–1838 (2004).

5. Guskov, A. et al. Cyanobacterial photosystem II at 2.9-Å resolution and the role of quinones, lipids, channels and chloride. *Nat. Struct. Mol. Biol*. **16**, 334–342 (2009).

6. Umena, Y. et al. Crystal structure of oxygen-evolving photosystem II at a resolution of 1.9 A. *Nature* **473**, 55–60 (2011).

7. Yano, J. et al. X-ray damage to the Mn4Ca complex in single crystals of photosystem II: a case study for metalloprotein crystallography. *Proc. Natl Acad. Sci. USA* **102**, 12047–12052 (2005).

8. Neutze, R. et al. Potential for biomolecular imaging with femtosecond X-ray pulses, *Nature*, **406**, 752-757 (2000).

9. Hirata, K. et al. A 1.9 Å resolution structure of 420 kDa cytochrome oxidase by femtosecond crystallography. *Nat. Methods* **11,** 734-736 (2014).

485   10 Suga, M. et al. Native structure of photosystem II at 1.95 A□ resolution viewed by

486   femtosecond X-ray pulses. *Nature* **517**, 99–103 (2015).

487   11 Suga, M. et al. Light-induced structural changes and the site of O=O bond

488   formation in PSII caught by XFEL. *Nature* **543**, 131–135 (2017).

489   12 Kern, J. et al. Structures of the intermediates of Kok's photosynthetic water

490   oxidation clock. *Nature* **563**, 421-425. (2018).

491   13 Suga, M. et al. An oxyl/oxo mechanism for oxygen-oxygen coupling in PSII

492   revealed by an X-ray free-electron laser. *Science* **366**, 334–338 (2019).

493   14 Ibrahim, M. et al. Untangling the sequence of events during the S2 → S3 transition

494   in photosystem II and implications for the water oxidation mechanism. *Proc. Natl*

495   *Acad. Sci. USA* **117**, 12624–12635 (2020).

496   15 Kato, Y. et al. Fourier transform infrared analysis of the S-state cycle of water

497   oxidation in the microcrystals of photosystem II. *J. Phys. Chem. Lett*. **9**, 2121-2126

498   (2018).

499   16 Flores, J.A. et al. Connexin-46/50 in a dynamic lipid environment resolved by

500   Cryo-EM at 1.9 Å. *Nature communications* **11**, 4331 (2020).

501   17 Nakane, T. et al. Single-particle cryo-EM at atomic resolution. Preprint at

502   https://doi.org/10.1101/2020.05.22.110189 (2020).

503   18 Yip, K.M. et al. Breaking the next Cryo-EM resolution barrier – Atomic resolution

504   determination of protein! Preprint at https://doi.org/10.1101/2020.05.21.106740

505   (2020).

506   19 Burmeister, W.P. Structural changes in a cryo-cooled protein crystal owing to radi-

507   ation damage. *Acta Crystal. D* **56**, 328–341 (2000).

508   20 Ravelli, R.B. et al. The "fingerprint" that X-rays can leave on structures. *Structure*

509   **8**, 315–328 (2000).

510   21 Weik, M. et al. Specific chemical and structural damage to proteins produced by

511   synchrotron radiation. *Proc. Natl. Acad. Sci. U.S.A.* **97**, 623–628 (2000).

512   22 Hamaguchi, T., Maki-Yonekura, S., Naitow, H., Matsuura, Y., Ishikawa, T. and

513   Yonekura, K. A new cryo-EM system for single particle analysis. *J. Struct. Biol.*

514   **207**, 40–48 (2019).

515   23 Rosenthal, P. B. and Henderson, R., Optimal determination of particle orientation,

516   absolute hand, and contrast loss in single-particle electron cryomicroscopy. *J. Mol.*

517   *Biol*. **333**, 721-45 (2003).

518   24 Koua, F.H.M., Umena, Y., Kawakami K. & Shen J.-R. Structure of Sr-substituted

519   photosystem II at 2.1 Å resolution and its implications in the mechanism of water

520   oxidation. *Proc. Natl. Acad. Sci. USA* **110,** 3889-3894 (2013).

521   25 Wang, J. Et al. Reduced occupancy of the oxygen-evolving complex of

522   photosystem II detected in cryo-electron microscopy maps. *Biochemistry* **57**,

523   5925-5929 (2018).

524   26 Yonekura, K. Electron crystallography of ultrathin 3D protein crystals: Atomic

525   model with charges. *Proc. Natl Acad. Sci. USA* **112**, 3368–3373 (2015).

526   27 Baker, L. A. Et al. Radiation damage in electron cryomicroscopy. *Methods in*

527   *Enzym.* **481**, 371-388 (2010).

528   28 Henderson, R. Cryo-protection of protein crystals against radiation damage in

529   electron and X-Ray diffraction. *Proc. R. Soc. Lond*. B **241**, 6-8 (1990).

530   29 Tanaka, A. et al. Two different structures of the oxygen-evolving complex in the

531   same polypeptide frameworks of photosystem II *J. Am. Chem. Soc*. **139**, 1728-1721

532   (2017).

533   30 Shen, J.-R., and Inoue, Y. Binding and functional properties of two new extrinsic

534   components, cytochrome *c*-550 and a 12 kDa protein, in cyanobacterial

535   photosystem II. *Biochemistry* **32,** 1825-1832 (1993).

536   31 Shen, J.-R., and Kamiya, N. Crystallization and the crystal properties of the

537   oxygen-evolving photosystem II from *Synechococcus vulcanus*. *Biochemistry* **39,**

538   14739-14744 (2000).

539   32 Shen, J.-R. et al. Purification and crystallization of oxygen-evolving photosystem II

540   core complex from thermophilic cyanobacteria. *Methods in Mol. Biol*. **684**, 41-51

541   (2011).

542   33 Zheng, S.Q. et al. MotionCor2: anisotropic correction of beam-induced motion for

543   improved cryo-electron microscopy. *Nat. Methods* **14**, 331-332 (2017).

544   34 Mindell, J.A., and Grigorieff, N. Accurate determination of local defocus and

545   specimen tilt in electron microscopy. *J Struct. Biol*. **142**, 334-347 (2003).

546   35 Scheres, S.H. RELION: implementation of a Bayesian approach to cryo-EM

547   structure determination. *J. Struct. Biol*. **180**, 519-530 (2012).

548   36 Grigorieff, N., and Harrison, S.C. Near-atomic resolution reconstructions of

549   icosahedral viruses from electron cryo-microscopy. *Curr. Opin. Struct. Biol*. **21**,

26

550   265-273 (2011).

551   37 Pettersen, E. F. et al. UCSF Chimera—a visualization system for exploratory

552   research and analysis. *J. Comp. Chem.* **25**, 1605-1612 (2004).

553   38 Emsley, P. et al. Features and development of Coot. *Acta Crystal. D* **66**, 486-501

554   (2010).

555   39 Adams, P. D. *et al.* PHENIX: a comprehensive Python-based system for

556   macromolecular structure solution. *Acta Crystal. D* **66**, 213-221 (2010).

557   40 Murshudov, G. N. *et al.* REFMAC5 for the refinement of macromolecular crystal

558   structures. *Acta Crystal. D* **67**, 355-367 (2011).

559   41 Pintilie, G. *et.al*. Measurement of atom resolvability in cryo-EM maps with

560   Q-scores. *Nat. Methods* **17**, 328-334 (2020).

561   42 Chen, V. B. *et al.* MolProbity: all-atom structure validation for macromolecular

562   crystallography. *Acta Crystal. D* **66**, 12-21 (2010).

563   43 Barad, B. A. *et al.* EMRinger: side chain–directed model and map validation for 3D

564   cryo-electron microscopy. *Nat. Methods* **12**, 943 (2015).

565   44 The PyMOL Molecular Graphics System, Version 2.1, Schrödinger, LLC.

566   45 Goddard, T.D. et al. UCSF ChimeraX: Meeting modern challenges in visualization

567   and analysis. *Protein Sci.* **27**, 14-25 (2018).

568   46 Winn, M. D. *et al.* Overview of the CCP4 suite and current developments. *Acta

569   Crystal. D* **67**, 235-242 (2011).

570   47 Kato K. et al. Structural basis for the adaptation and function of chlorophyll *f* in

571   photosystem I. *Nat. Commun.* **11**, 1-10 (2020).

27
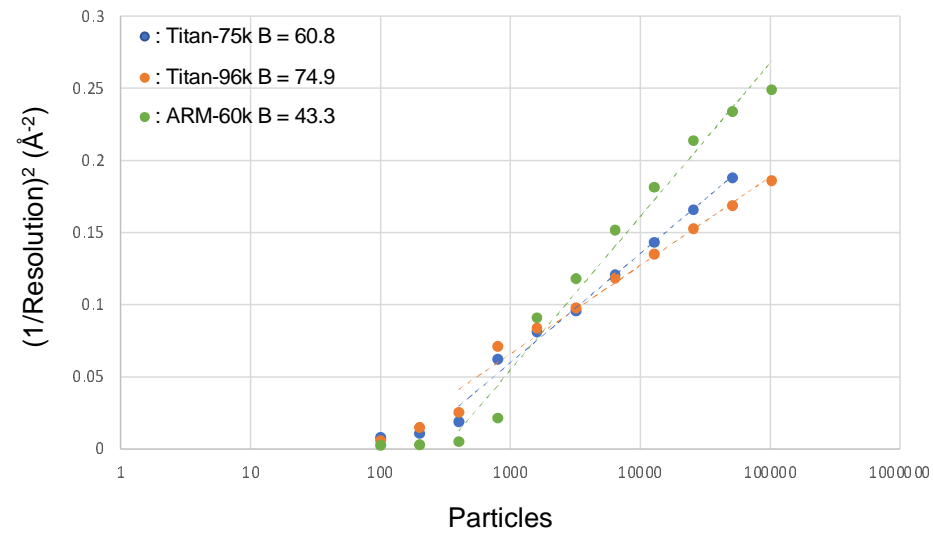
572   48

573   49   **Fig. 1 B-factor plot for the data sets of Titan-75k, Titan-96k and ARM-60k.** B

574   factor plot for the Titan-75k data set at a dose of 40 e$^-$ Å^{-2} (blue), the Titan-96k data

575   set at a dose of 40 e$^-$ Å^{-2} (orange), and the ARM-60k data set at a dose of 83 e$^-$ Å^{-2}

576   (green).

577   50

578
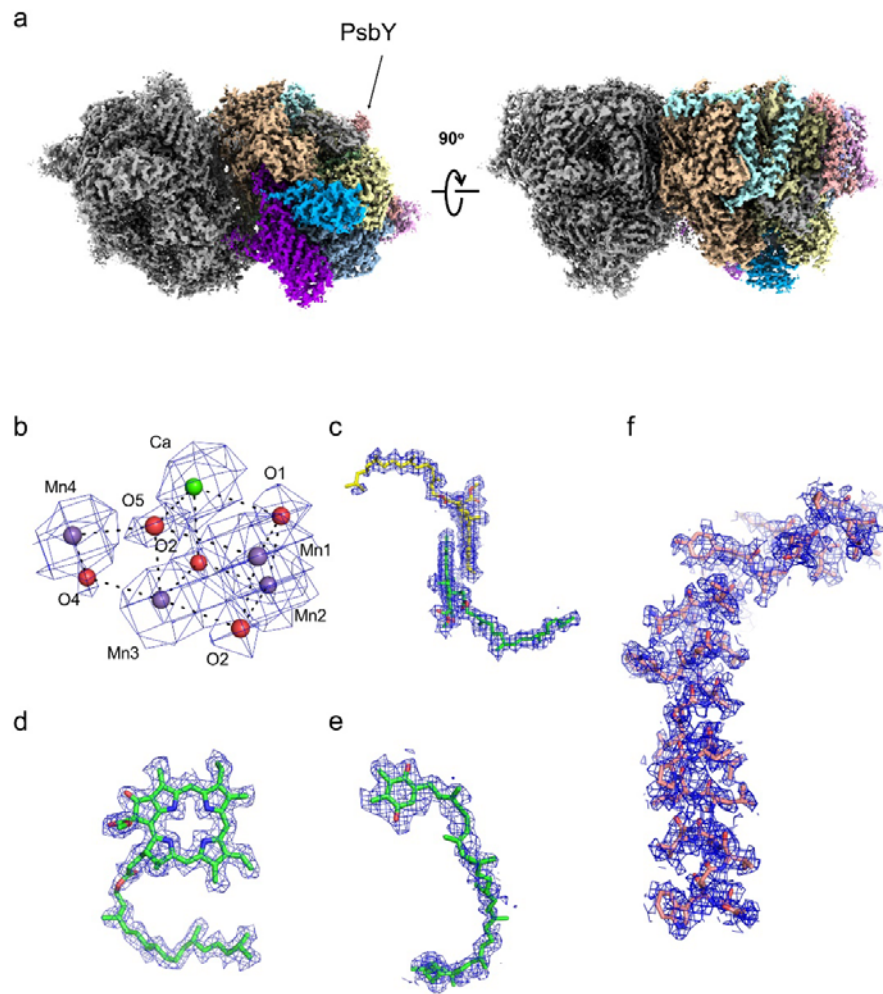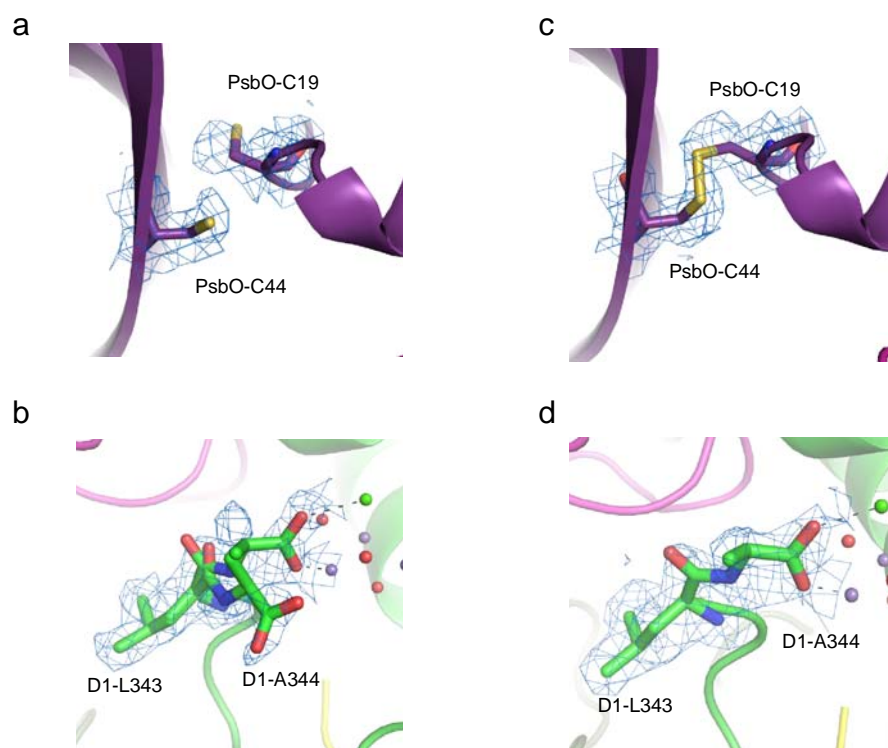579 **Fig. 2 Overall structure of PSII at a high-dose**. **a** The cryo-EM density of the PSII at

580 1.95 Å resolution from the ARM-60k data set. **b**-**e** The cryo-EM density of cofactors,

581 OEC (**b**), P680 (**c**), pheophytin (**d**) and plastoquinone (Q_B) (**e**), superposed with the

582 refined model. **f** The density of PsbY superposed with the refined model. The densities

583 were depicted at 5 σ.

584

585

29

a

PsbO-C19

PsbO-C44

c

PsbO-C19

PsbO-C44

b

D1-L343   D1-A344

d

D1-A344

D1-L343

586

Fig. 3 Electron beam damages in the PSII structure of the ARM-60k data set at the high-dose (83 e⁻ Å⁻²) and low-dose (3.3 e⁻ Å⁻²). a The broken disulfide bond in PsbO at the high-dose. **b** The alternative conformation at D1-A344 at the high dose. **c** The disulfide bond recovered in PsbO at the low-dose. **d** The single conformation of D1-A344 at the low dose. The densities were depicted at 5 σ.

592

593

594
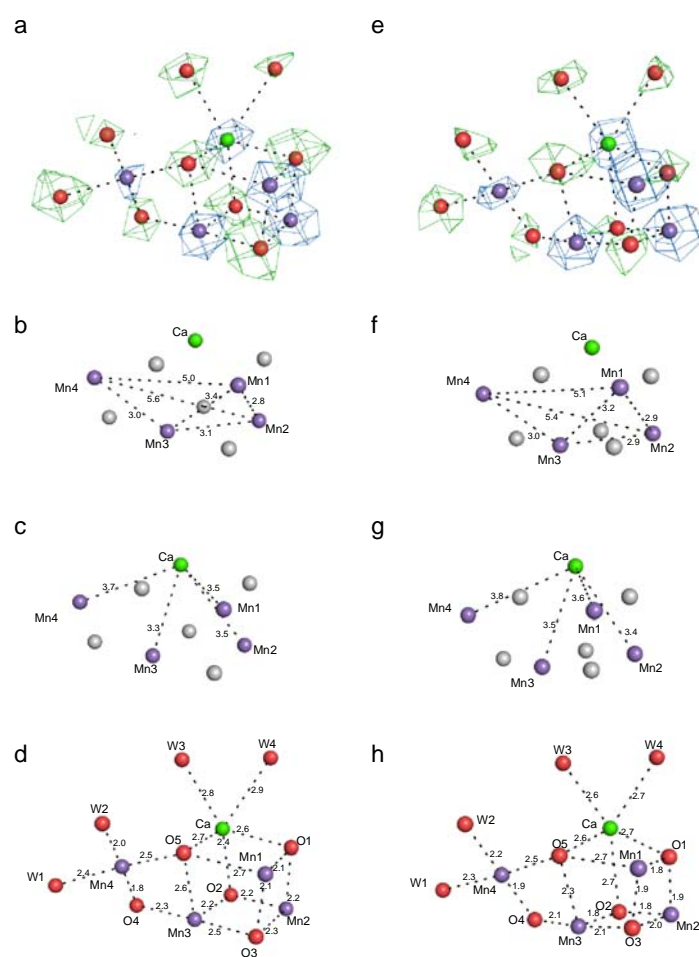
Fig. 4 Electron beam damages in the OEC structure solved at the high-dose (83 e⁻ Å⁻²) and low-dose (3.3 e⁻ Å⁻²). a-d: High dose structure. **a** The cryo-EM density (blue) for manganese and calcium atoms at 17 σ and the subtracted map (green) for oxygen atoms and water molecules at 7 σ. **b** Mn−Mn distances in the OEC (in Å). **c** Mn−Ca distances in the OEC (in Å) **d** Mn−O, Ca−O, Mn−water and Ca−water distances in the OEC (in Å). **e-h:** Low dose structure. **e** The cryo-EM density (blue) for manganese and calcium atoms at 17 σ and the subtracted map (green) for oxygen atoms and water

602   molecules at 7 σ. **f** Mn−Mn distances in the OEC (in Å). **g** Mn−Ca distances in the OEC

603   (in Å). **h** Mn−O, Ca−O, Mn−water and Ca−water distances in the OEC (in Å).
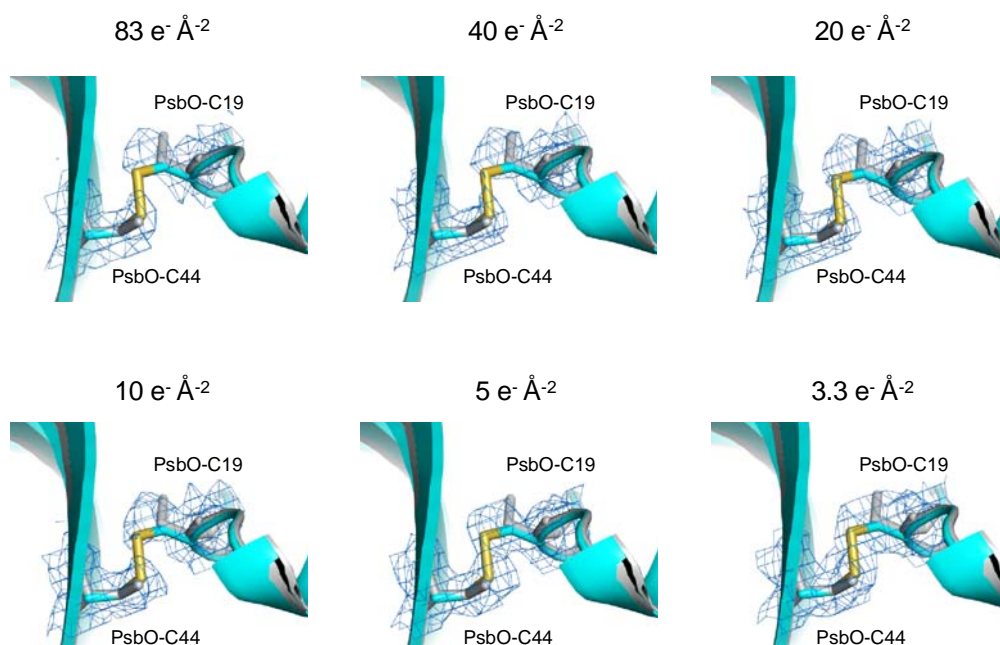
604

605   **Fig. 5 Changes of the cryo-EM map in the region of the disulfide bond in PsaO**
606   **with changes of the electron beam dose.** The cryo-EM maps for each electron dose are
607   displayed as a blue mesh at 4 σ and the corresponding models for low-dose (colored)
608   and high-dose (gray) are shown as sticks.

609

610   **Table 1 Sample preparation and Cryo-EM data collection parameters.**

Data set	Titan-75K	Titan-96K	ARM-60K
Original sample conc.	3.8 Chl mg/ml	9.7 Chl mg/ml	9.7 Chl mg/ml
Original sample buffer	20 mM MES (pH6.0), 5% glycerol, 0.04% β-DDM	20 mM MES (pH6.0)	20 mM MES (pH6.0)
Dilution buffer	20 mM MES (pH6.0), 0.04% β-DDM	20 mM MES (pH6.0)	20 mM MES (pH6.0)
Dilution	10-fold	5-fold	5-fold
Final sample conc.	0.38 Chl mg/ml	1.94 Chl mg/ml	1.94 Chl mg/ml
Data collection and processing			
Microscope	Titan Krios	Titan Krios	CRYO ARM 300
Detector	Falcon3EC in EC mode	Falcon3EC in EC mode	Gatan K2 summit in Counting mode
Magnification	75K	96K	60K
Voltage (kV)	300	300	300
Defocus range (μm)	-1.00 to -2.00	-1.00 to -2.50	-0.8 to -1.6
Pixcel size (Å)	0.870	0.678	0.822
Total electron dose ($Å^2$)	40	40	83
Exposure time (s)	45.11	24.64	10
Number of frames per image	78	39	50
Number of micrographs	2,084	4,237	2,160
Initial particle images	354,233	612,287	444,729
Final particle images	90,897	203,912	174,099
Map resolution (Å)	2.23 (2.22)*	2.26 (2.20)*	1.98 (1.95)*
Map sharpening B-factor ($Å^2$)	-54 (-53)*	-60 (-56)*	-34 (-32)*
Rosenthal-Henderson B factor ($Å^2$)	60.8	74.9	43.3
Applied symmetry	C2	C2	C2

611   * After micelle-density subtraction

612

613 **Table 2 Statistics of data collection, processing and refinement.**

614

Refinement	High-dose	Low-dose
PDB ID	7D1T	7D1U
EMDB ID	EMD-30547	EMD-30548
Initial Model used (PDB code)	3WU2	3WU2
Model resolution (Å)	1.94	2.03
FSC threshold	0.5	0.5
No. of atoms		
Protein	41708	41680
Ligand	8854	8854
Water	2432	2121
B factors (Å^2)		
Protein	20.6	21.2
Ligand	23.5	24.1
Water	26.4	23.7
R.m.s deviations		
Bond lengths (Å)	0.012	0.010
Bond angles (°)	1.46	1.31
Validation		
MolProbity score	1.3	1.5
Clashscore	1.8	2.2
Poor rotamers (%)	2.4	3.1
EMRinger score	7.0	6.8
Q-Score	0.87	0.86
Ramachandran plot		
Favored (%)	97.93	97.55
Allowd (%)	1.88	2.26
Disallowed (%)	0.19	0.19

615

616

617

618

619

620 **Table 3 Summarization of the distances of atoms of the Mn$_4$CaO$_5$ cluster.**

	High-dose (Average)	Low-dose (Average)	SR (3WU2) (Average)	XFEL (4UB6) (Average)	High-dose 4th	3rd	2nd	1st	Initial	Low-dose 4th	3rd	2nd	1st	Initial
Mn1-Mn2	2.8	2.9	2.8	2.7	2.81	2.83	2.82	2.82	2.81	2.88	2.87	2.89	2.8	2.95
Mn1-Mn3	3.4	3.2	3.3	3.2	3.35	3.36	3.35	3.36	3.46	3.20	3.20	3.24	3.18	3.37
Mn1-Mn4	5.0	5.1	5	5	5.04	5.02	5.03	5.03	4.99	5.10	5.09	5.08	5.04	5.32
Mn2-Mn3	3.1	2.9	2.9	2.7	3.08	3.10	3.09	3.09	3.06	2.88	2.88	2.88	2.85	2.75
Mn2-Mn4	5.6	5.4	5.4	5.2	5.65	5.65	5.65	5.63	5.42	5.47	5.46	5.42	5.43	5.40
Mn3-Mn4	3.0	3.0	3.0	2.9	2.97	2.97	2.98	2.94	2.67	3.04	3.03	3.01	3.00	3.05
Mn1-Ca	3.5	3.6	3.5	3.5	3.55	3.52	3.52	3.52	3.51	3.59	3.57	3.55	3.56	3.83
Mn2-Ca	3.5	3.4	3.4	3.3	3.49	3.45	3.46	3.46	3.29	3.44	3.43	3.41	3.44	3.35
Mn3-Ca	3.3	3.5	3.4	3.4	3.32	3.29	3.28	3.27	3.04	3.45	3.45	3.44	3.46	3.43
Mn4-Ca	3.7	3.8	3.8	3.8	3.73	3.69	3.70	3.68	3.57	3.76	3.76	3.70	3.80	3.86
Mn1-O1	2.1	1.8	1.9	1.8	2.11	2.10	2.08	2.06	2.34	1.80	1.76	1.77	1.78	2.09
Mn1-O3	2.1	1.9	1.8	1.9	2.09	2.10	2.10	2.09	2.29	1.89	1.90	1.91	1.92	1.90
Mn1-O5	2.7	2.7	2.6	2.7	2.72	2.73	2.74	2.75	2.64	2.71	2.72	2.72	2.72	2.89
Mn2-O1	2.2	1.9	2.1	1.8	2.18	2.17	2.17	2.16	2.19	1.98	1.95	1.92	1.86	2.12
Mn2-O2	2.2	1.8	2.1	1.8	2.24	2.23	2.2	2.17	2.45	1.84	1.83	1.82	1.80	2.45
Mn2-O3	2.3	2.0	2.1	2.0	2.28	2.28	2.27	2.26	2.36	2.01	2.01	2.01	2.00	1.95
Mn3-O2	2.2	1.8	1.9	1.9	2.18	2.18	2.16	2.14	2.04	1.80	1.78	1.81	1.86	2.08
Mn3-O3	2.5	2.1	2.1	2.1	2.48	2.47	2.44	2.42	2.48	2.05	2.06	2.06	2.07	2.02
Mn3-O4	2.3	2.1	2.1	1.9	2.30	2.30	2.28	2.26	2.38	2.17	2.11	2.05	1.96	2.71
Mn3-O5	2.6	2.3	2.4	2.2	2.58	2.58	2.56	2.54	2.58	2.35	2.32	2.29	2.23	2.57
Mn4-O4	1.8	1.9	2.1	2.0	1.80	1.80	1.79	1.82	1.96	1.86	1.89	1.92	1.97	2.05
Mn4-O5	2.5	2.5	2.5	2.3	2.49	2.46	2.45	2.44	2.59	2.5	2.48	2.45	2.40	2.67
Mn4-W1	2.4	2.3	2.2	2.3	2.38	2.40	2.39	2.40	2.54	2.31	2.32	2.36	2.32	2.33
Mn4-W2	2.0	2.2	2.2	2.1	2.05	2.03	2.03	2.07	2.11	2.18	2.18	2.18	2.15	1.84
Ca-O1	2.6	2.7	2.4	2.6	2.63	2.63	2.62	2.62	2.60	2.72	2.70	2.67	2.63	2.47
Ca-O2	2.4	2.7	2.5	2.7	2.39	2.39	2.41	2.43	2.41	2.67	2.68	2.69	2.71	2.73
Ca-O5	2.7	2.6	2.7	2.5	2.71	2.70	2.68	2.66	2.70	2.62	2.60	2.58	2.55	2.60
Ca-W3	2.8	2.6	2.4	2.6	2.76	2.79	2.78	2.78	2.80	2.56	2.56	2.57	2.53	2.64
Ca-W4	2.9	2.7	2.5	2.5	2.89	2.93	2.92	2.94	2.92	2.71	2.71	2.73	2.65	2.71

621
622
623